Supplementary material to

# Structural and spectroscopic characterization of brownmillerite type $Ca_2Fe_{2-x}Ga_xO_5$ solid solution series.

# 1 The Brownmillerite Structure

The Brownmillerite structure can be expressed as $A_2B'_xB_{2-x}O_5$, where A = alkaline-earth metals (e.g. Ca, Sr, Ba) and B'/B = group III or transition-metal atoms (e.g. Al, Ga, Cr, Mn, Co, Fe, In) (Grosvenor *et al.*, 2009, Bielecki *et al.*, 2014). Compared to the parent perovskite sub-cell the lattice parameters of the orthorhombic Brownmillerite are $a \approx c \approx \sqrt{2} \cdot a_p$ and $b \approx 4 \cdot a_p$. As shown in Fig. S1 the structural building units consists of alternating layers of corner-sharing $BO_6$ octahedra and chains of corner-sharing $B'O_4$ tetrahedra. The alkaline earth metals are located in the interstitial space between the layers, which are stacked perpendicular to the **b**-axis (Redhammer *et al.*, 2005). The tetrahedra chains parallel to the **c**-axis arise from vacant anion positions running along [1 1 0] at the perovskite sub-cell (Figure S1) (Abakumov *et al.*, 2005).

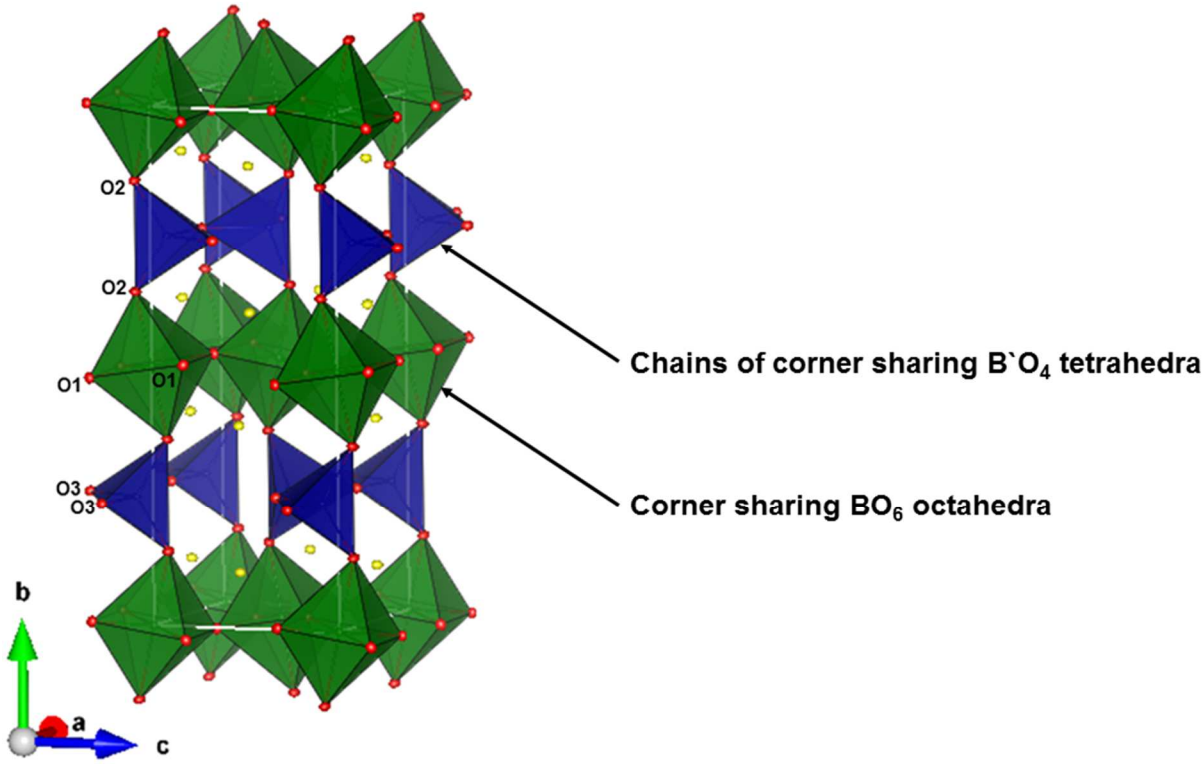


**Figure S1.** Plot of the Brownmillerite structure $Ca_2B'_xB_{2-x}O_5$ (*Pnma*).

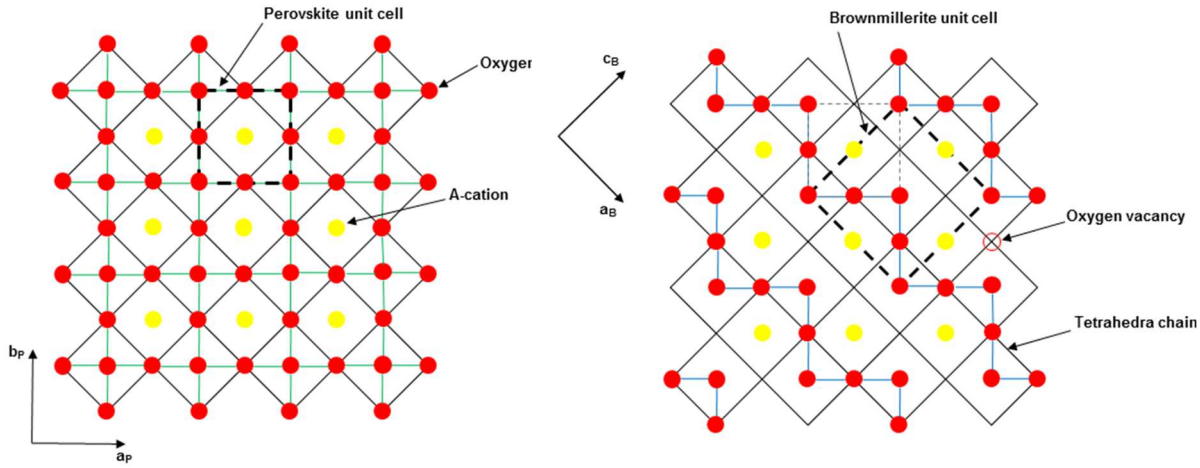


**Figure S2.** Octahedral layer of the ideal Perovskite structure, perpendicular to the $\mathbf{c_P}$-axis (left side) and tetrahedral chains of the ideal Brownmillerite structure, perpendicular to the $\mathbf{b_B}$-axis (right side).

Differences in chemical composition and temperature cause polyhedron distortion, octahedral tilting and twisting of the tetrahedra chains. The twisting of the tetrahedra around the **b**-axis, with an alternating sense of rotation along one single chain, is leading to arbitrarily termed L- or R-handed chains (Fig. S4). The space group of the Brownmillerite structure depends exclusively on the symmetry relation between the L- and R-handed chains (Fig. S5). The most common space groups are *I2mb* (46), *Pnma* (62) and *Imma* (74), with regard to unit cell settings where $b > c > a$ (used in this work) (Abakumov *et al.*, 2005, Tilley, 2016).

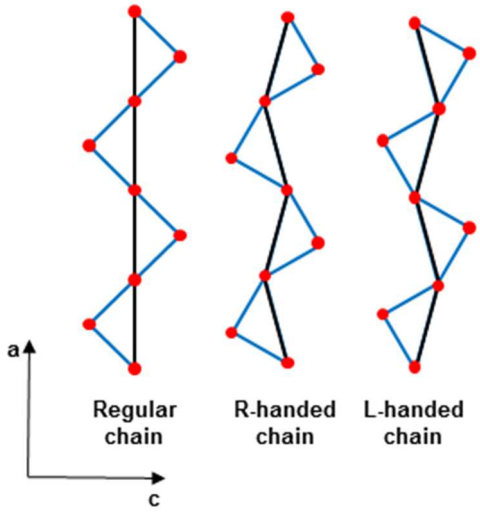


**Fig. S3.** Twisting of the tetrahedra around the b-axis result in arbitrarily termed L- and R-handed chains.

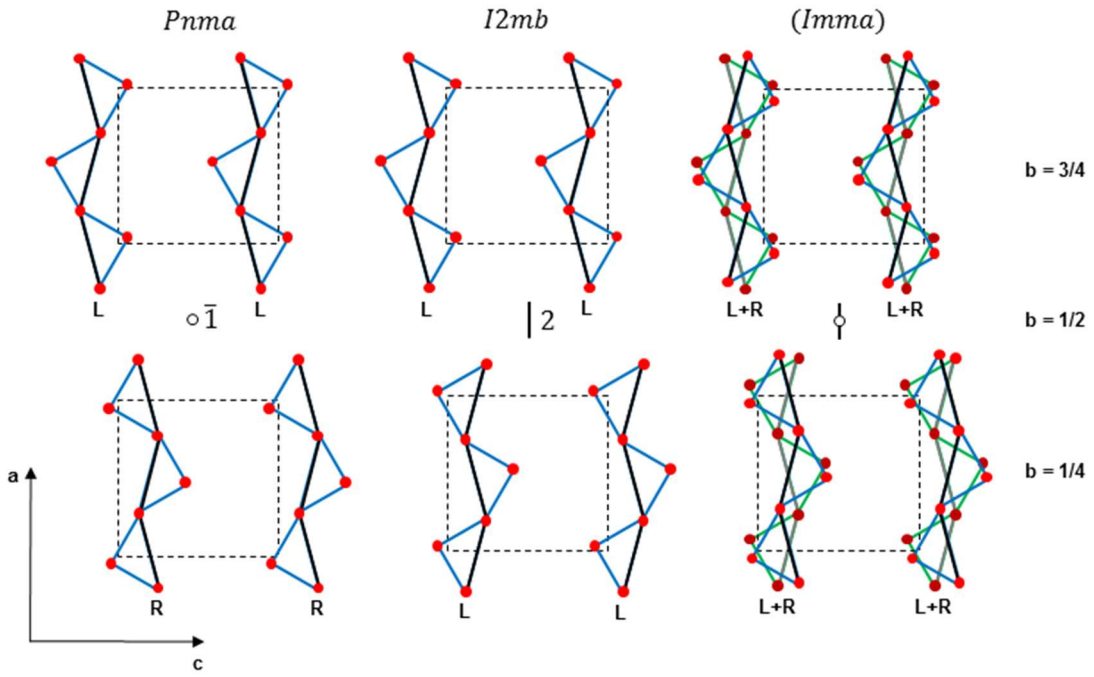


**Fig. S4.** Symmetry relations between the tetrahedra chains

In case that all tetrahedral chains have the same orientation throughout the structure, only L- or R-handed chains are present, the layers of tetrahedra are related to each other by twofold axis along **c**. This Brownmillerite structure can be described with the non-centrosymmetric space-group *I*2*mb*. In contrast, when L- and R-handed chains are alternating along the **b**-axis, the structure is consistent with the centrosymmetric space group *Pnma*. The third of the above-mentioned space groups *Imma* is used for randomly disordered arrangements of L- and R-handed chains, characterized by the absence of octahedra and tetrahedra rotation (Tilley, 2016, Piovano *et al.*, 2015, Young & Rondinelli, 2015).

In some cases, the ordering of L- and R- handed chains can also be more complex, which will require a four-dimensional super space description. A more detailed specification of this structure will not be written here, for further information see the recently published book "Perovskites: Structure-Property Relationships" by Richard J. D. Tilley or the PhD thesis "Ordering of tetrahedral chains in layer-like structures periodic and aperiodic examples" by Hannes Krüger (Tilley, 2016, Krueger, 2007).

Over the past years a variety of Brownmillerites with differing chemical composition were synthesized and subsequently characterized by a combination of diffraction-, spectroscopic- and theoretical-methods. However, it has not yet been possible to explain the driving force of

the different tetrahedral chain ordering or the transformation of the L-handed chain into the R-handed chain and vice versa.

The cubic perovskite-type structure has the chemical formula $ABO_3$. The crystal structure can be described as follows: Each B cation is octahedrally coordinated with six oxygen atoms and the A cation occupying the 12-fold coordination site formed in the middle of the corner sharing octahedra. The cubic perovskite-type structure belongs to the space group $Pm\bar{3}m$ and possesses a very high degree of compositional flexibility. The exchange of the atoms may lead to a distortion of the structure due to size and Jahn-Teller effects. It is also possible to synthesize perovskites with different oxygen stoichiometry, regarded as perovskite related compounds. Oxygen-defect perovskites $ABO_{3-\delta}$ with oxygen stoichiometry 2.5 to 3.0 result from B cations with a lower oxidation state. If the B cation can be present with another coordination than octahedral, e.g. coordinated to five (square pyramidal) or four (tetrahedral or square planar) oxygen atoms, a vacancy ordered structure may form. One possible vacancy-ordered structure is the Brownmillerite structure (Okrusch, 2014, Stølen *et al.*, 2006).

## 2 Synthesis

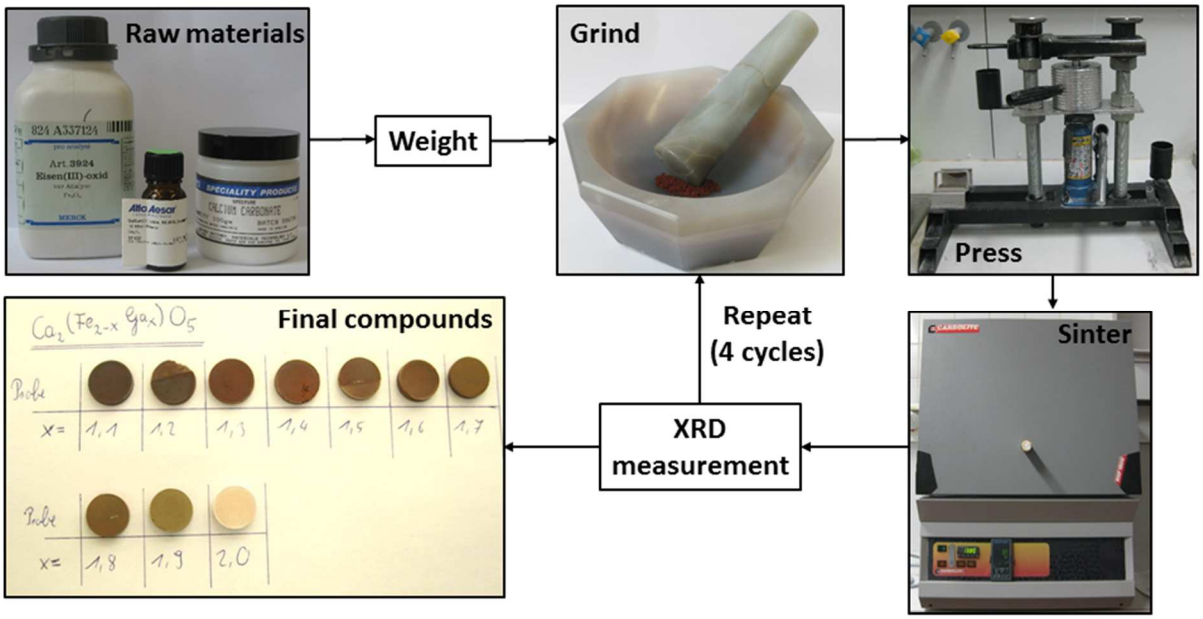


**Figure S5.** Flowchart for the procedure of preparing polycrystalline powders by solid-state ceramic sintering technique.

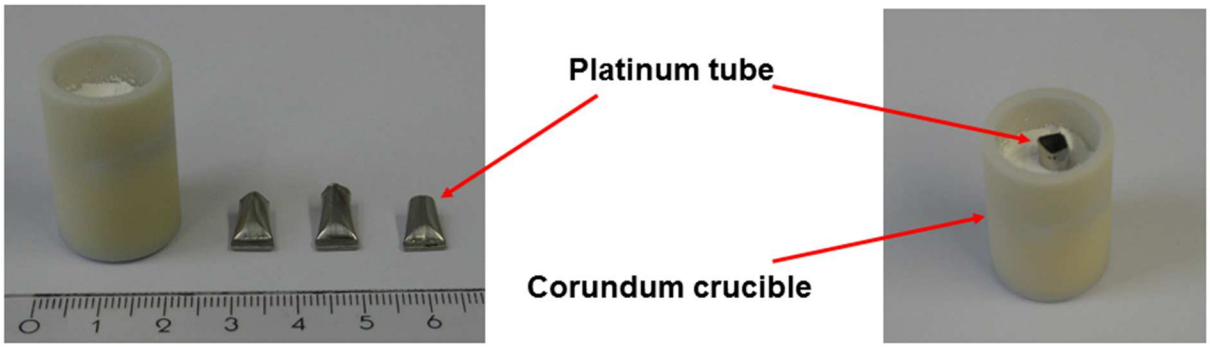


**Figure S6.** The preparation of $Ca_2Fe_{2-x}Ga_xO_5$ samples in small platinum tubes for crystal growth by slow cooling of melts.

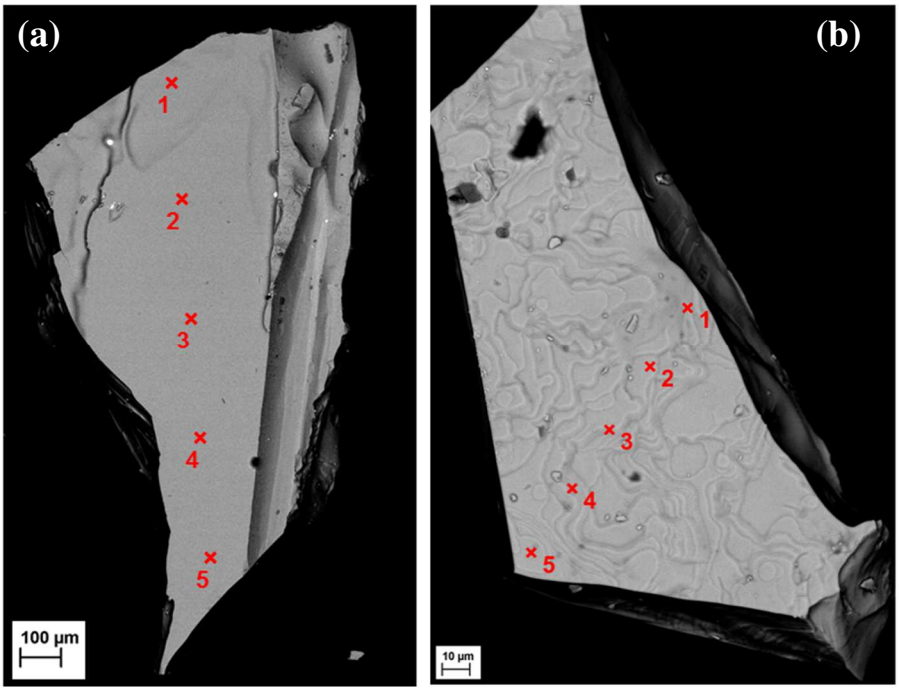


**Figure S7**. SEM-BSE image a selected $Ca_2Fe_{2-x}Ga_xO_5$ single crystals (a) with x = 0.2, and (b) x = 1.5, synthesized by slow cooling of melts. The red crosses mark the measuring points of the EDX analyses.

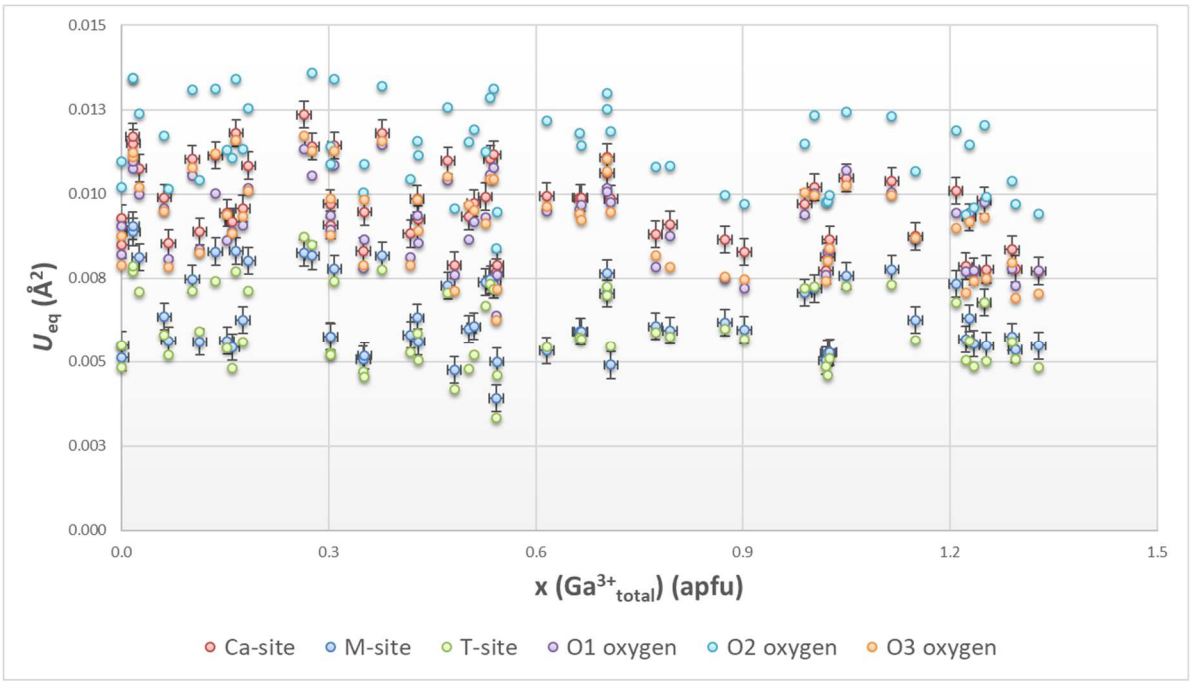


**Figure S8:** Variation in equivalent atomic displacement parameters for the individual crystallographic sites within the $Ca_2Fe_{2-x}Ga_xO_5$ solid solution series

# 3 Detailed outline of structural variations in bond lengths and bond angles

## 3.1 The octahedral site:

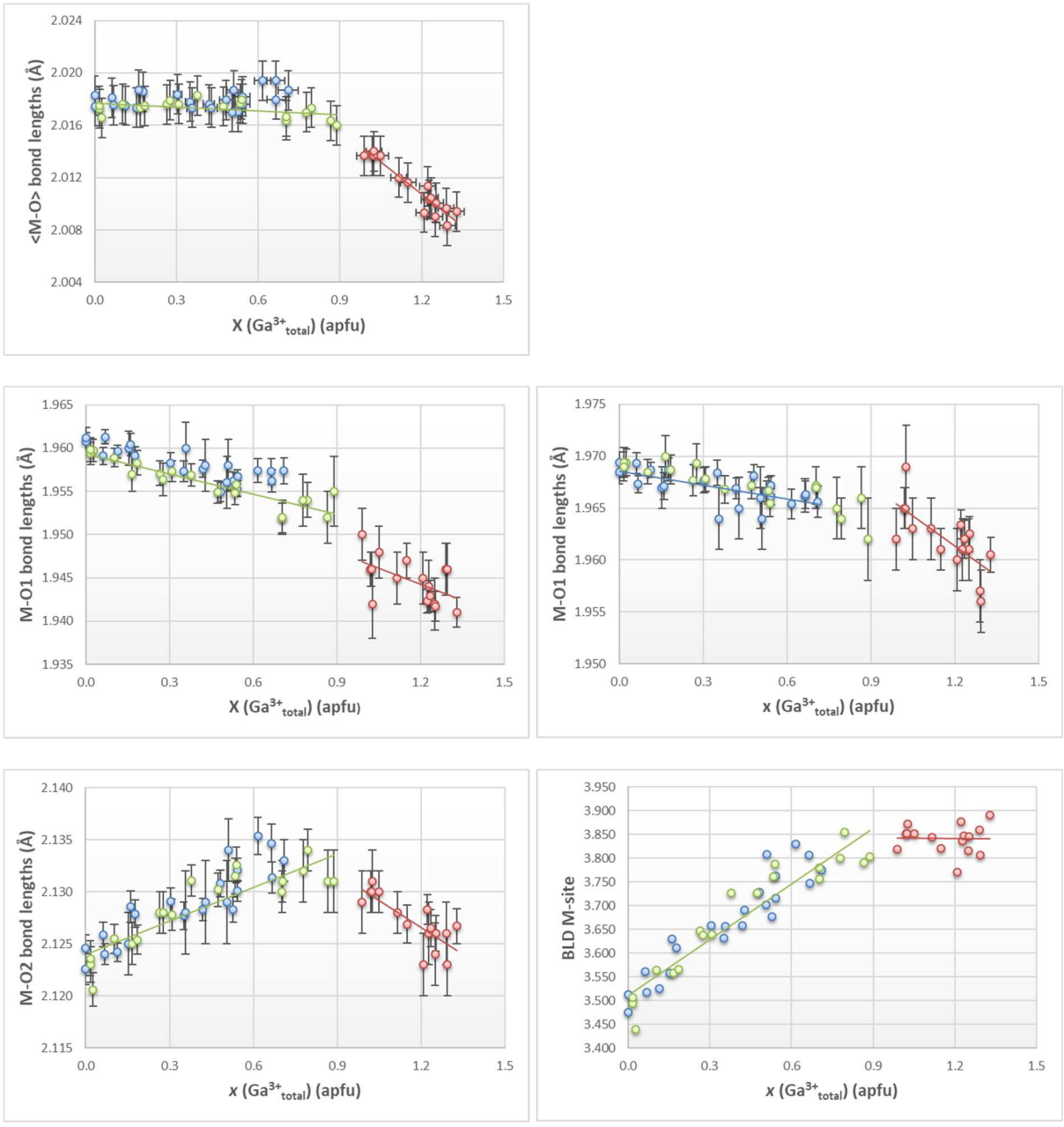


**Figure S9:** Average (A) and individual M-O bond lengths (B-D) as well as bond length distortion (BLD) values for the $Ca_2Fe_{2-x}Ga_xO_5$ solid solution series at 25 °C. Linear regression curves are fitted to the data and serve as guides to the eye; blue circles represent data for samples synthesized by flux growth, green circles data for samples synthesized by slow cooling of melts in the *Pnma*, while red circles data in the *I2mb* phase.

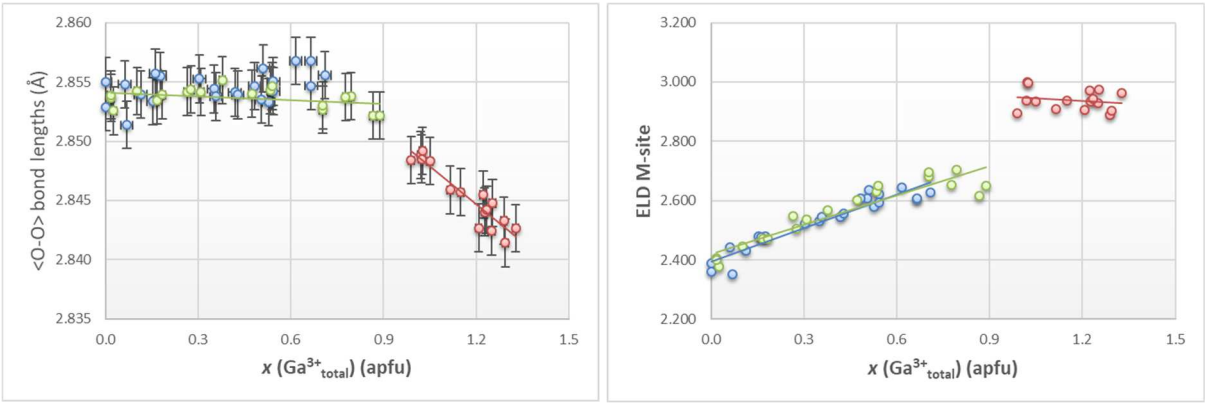


**Figure S10.** Average O-O atom distances, defining the edge of the $(Fe^{3+},Ga^{3+})O_6$ octahedron as well as edge length distortion (ELD) values for the $Ca_2Fe_{2-x}Ga_xO_5$ solid solution series at 25 °C. Linear regression curves are fitted to the data and serve as guides to the eye; blue circles represent data for samples synthesized by flux growth, green circles data for samples synthesized by slow cooling of melts in the *Pnma*, while red circles data in the *I*2*mb* phase

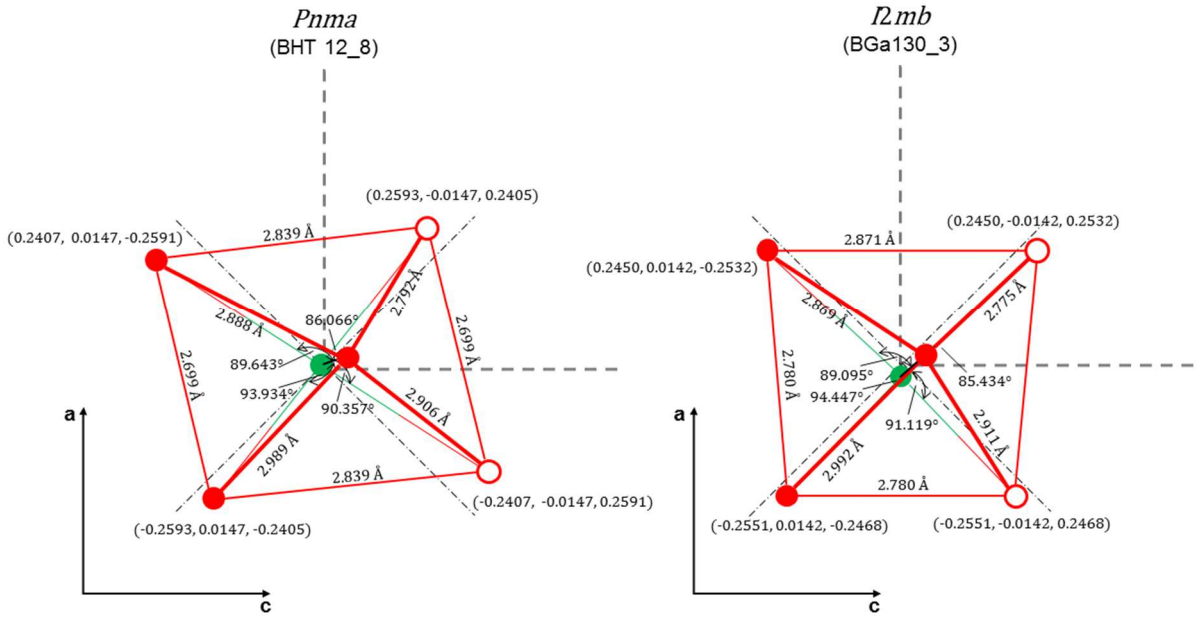


**Figure S11.** Illustration of the octahedra including O1, O2 and M-site positions of samples BHT12_8 (*Pnma*, x = 0.902) and BGa130_3 (*I*2*mb*, x = 0.989), with the most relevant bond lengths and angles.

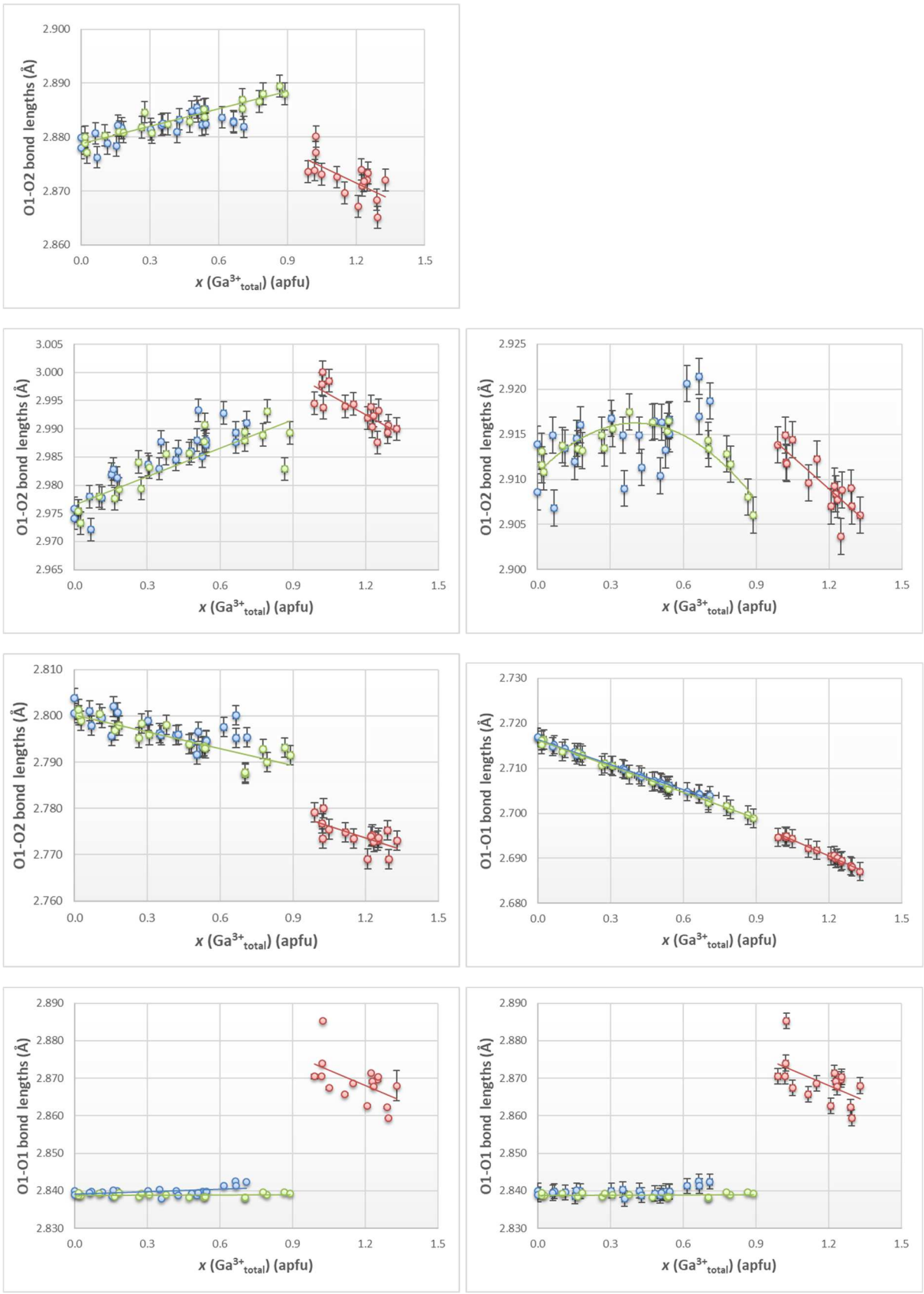


**Figure S12.** Individual O-O atom distances, defining the edge of the $(Fe^{3+},Ga^{3+})O_6$ octahedron for the $Ca_2Fe_{2-x}Ga_xO_5$ solid solution series at 25 °C. Symbols as in S9.

## 3.2 The tetrahedral site

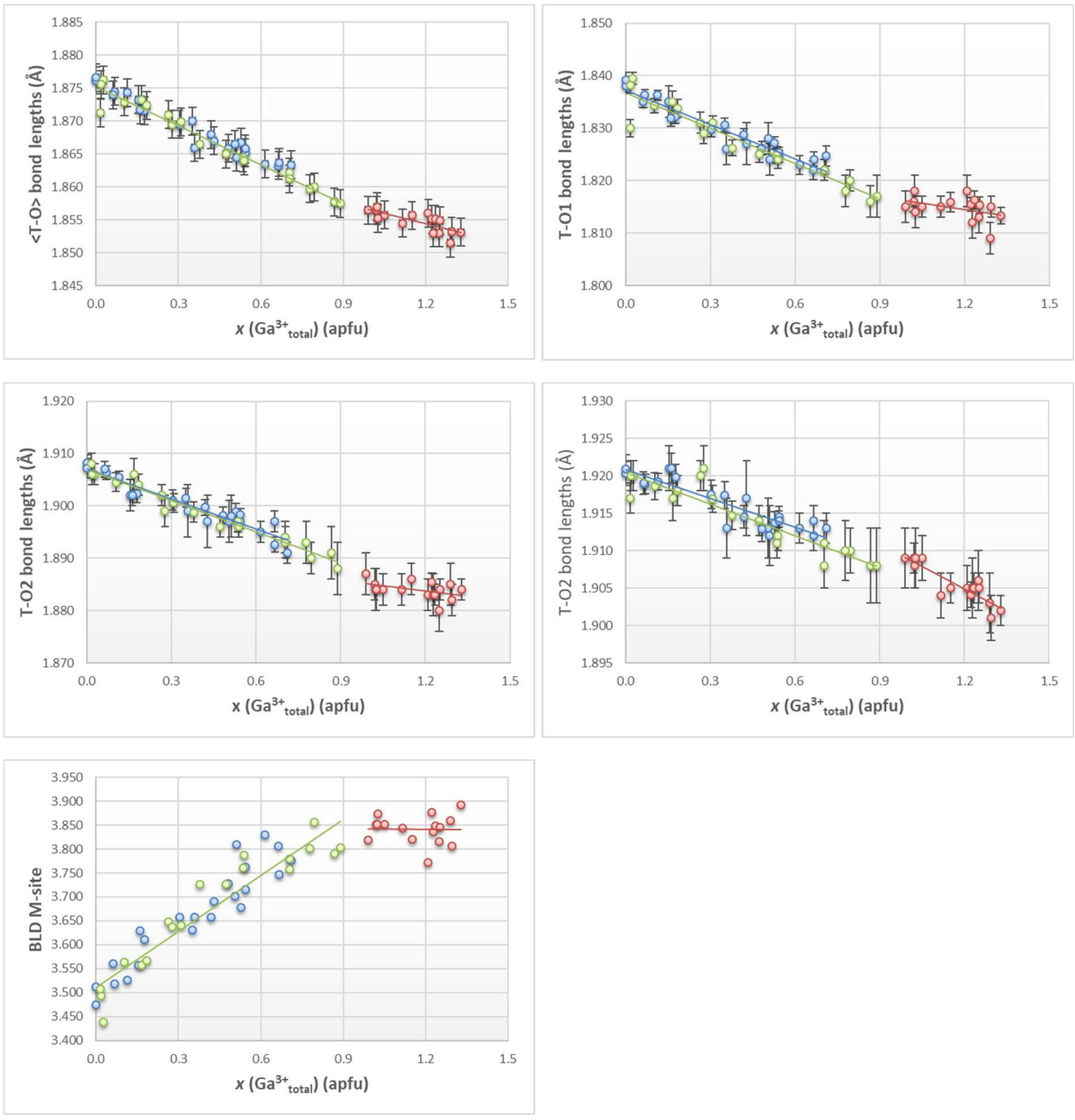


**Figure S13:** Average (A) and individual T-O bond lengths (B-D) as well as bond length distortion (BLD) values for the $Ca_2Fe_{2-x}Ga_xO_5$ solid solution series at 25 °C, symbols as in S9.

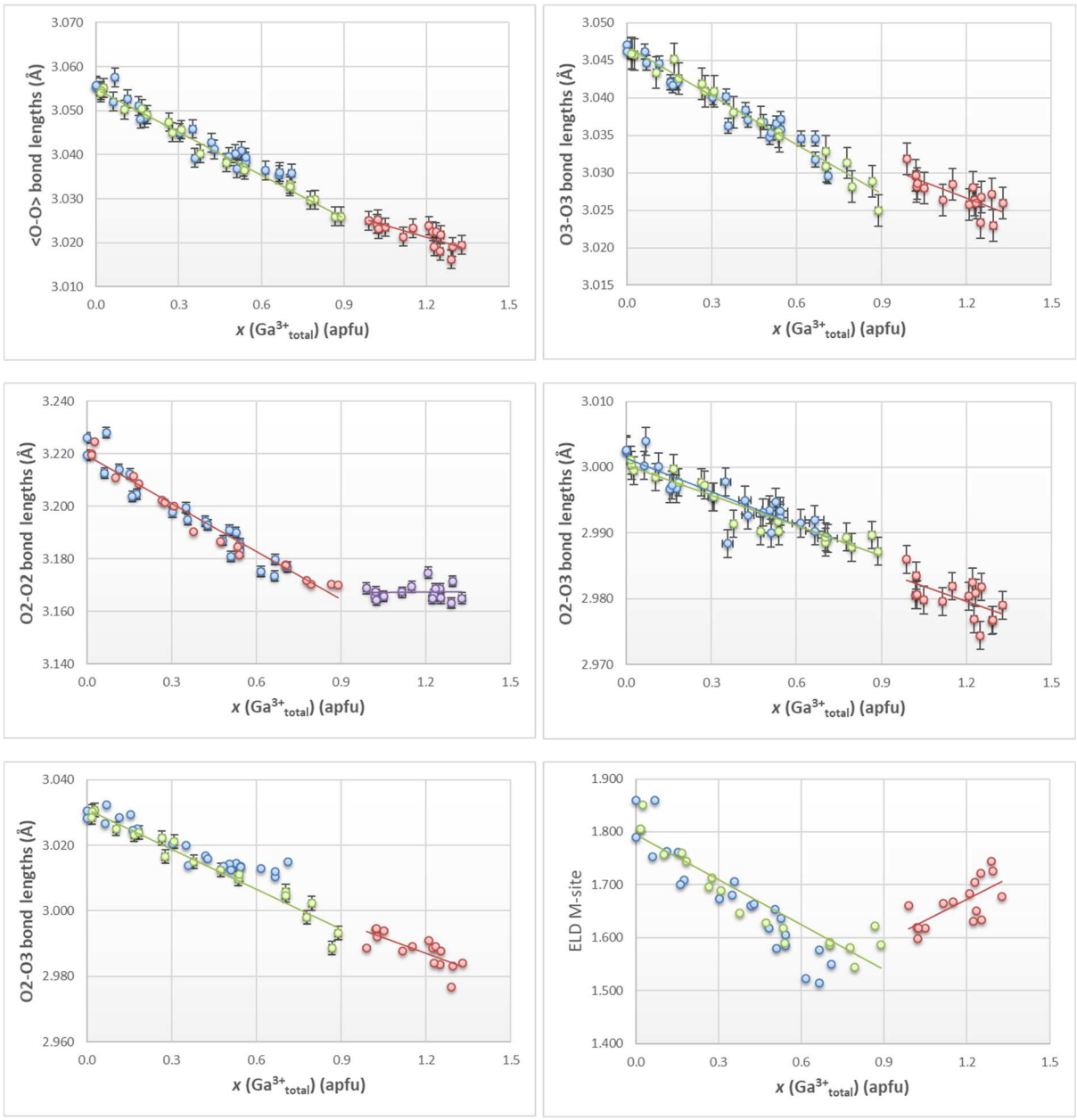


**Figure S14:** Average (A) and individual O-O atom distances (B-E), defining the edge of the $(Fe^{3+},Ga^{3+})O_6$ tetrahedron as well as edge length distortion (ELD) for the $Ca_2Fe_{2-x}Ga_xO_5$ solid solution series at 25 °C, symbols as in S9.

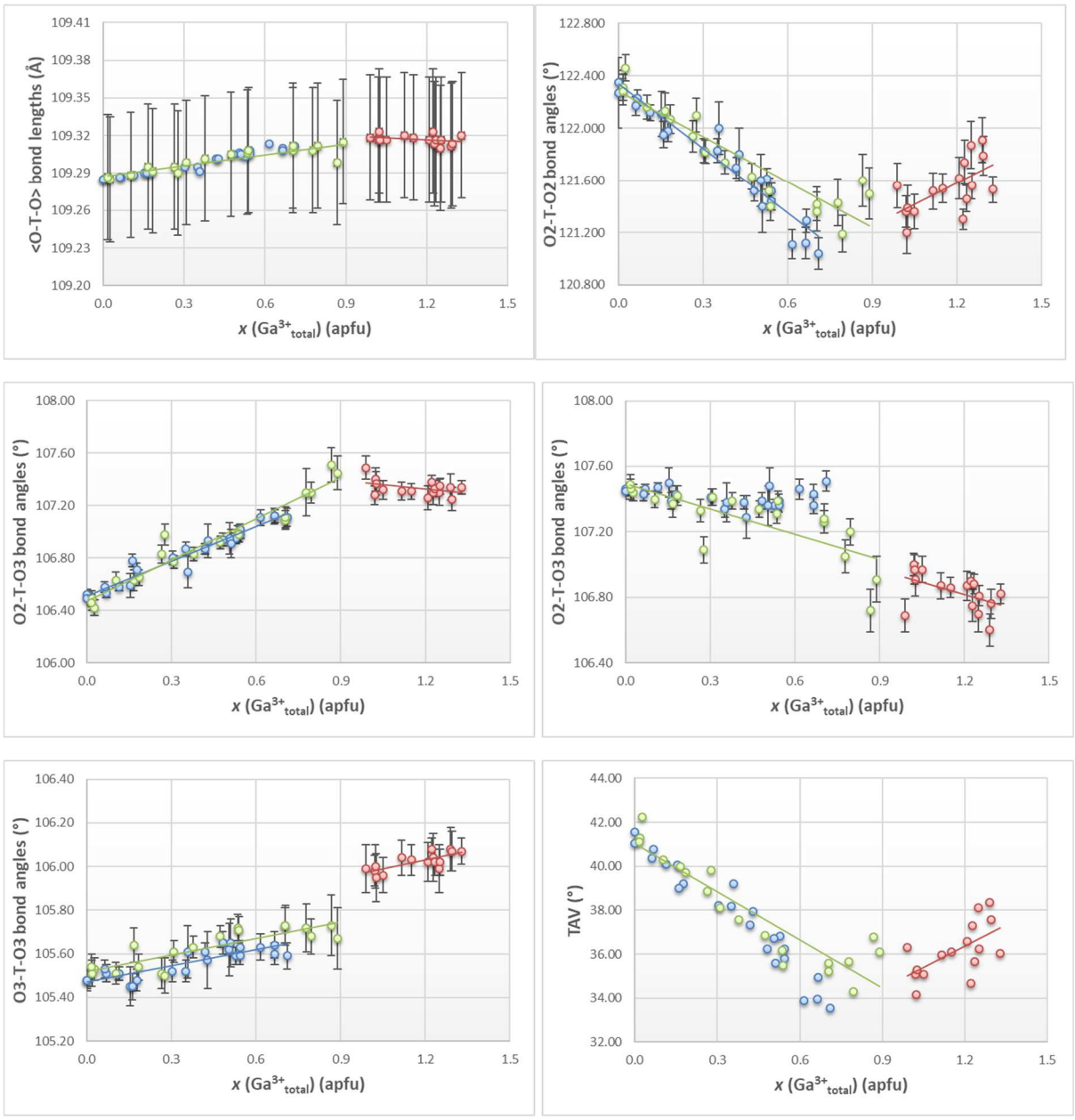


**Figure S15.** Average (A) and individual O-T-O bond angles (B-E) as well as quadratic tetrahedral angle variance (TAV, Robinson et. al. 1971) for the $Ca_2Fe_{2-x}Ga_xO_5$ solid solution series at 25 °C.

### 3.3 The interstitial $Ca^{2+}$ site

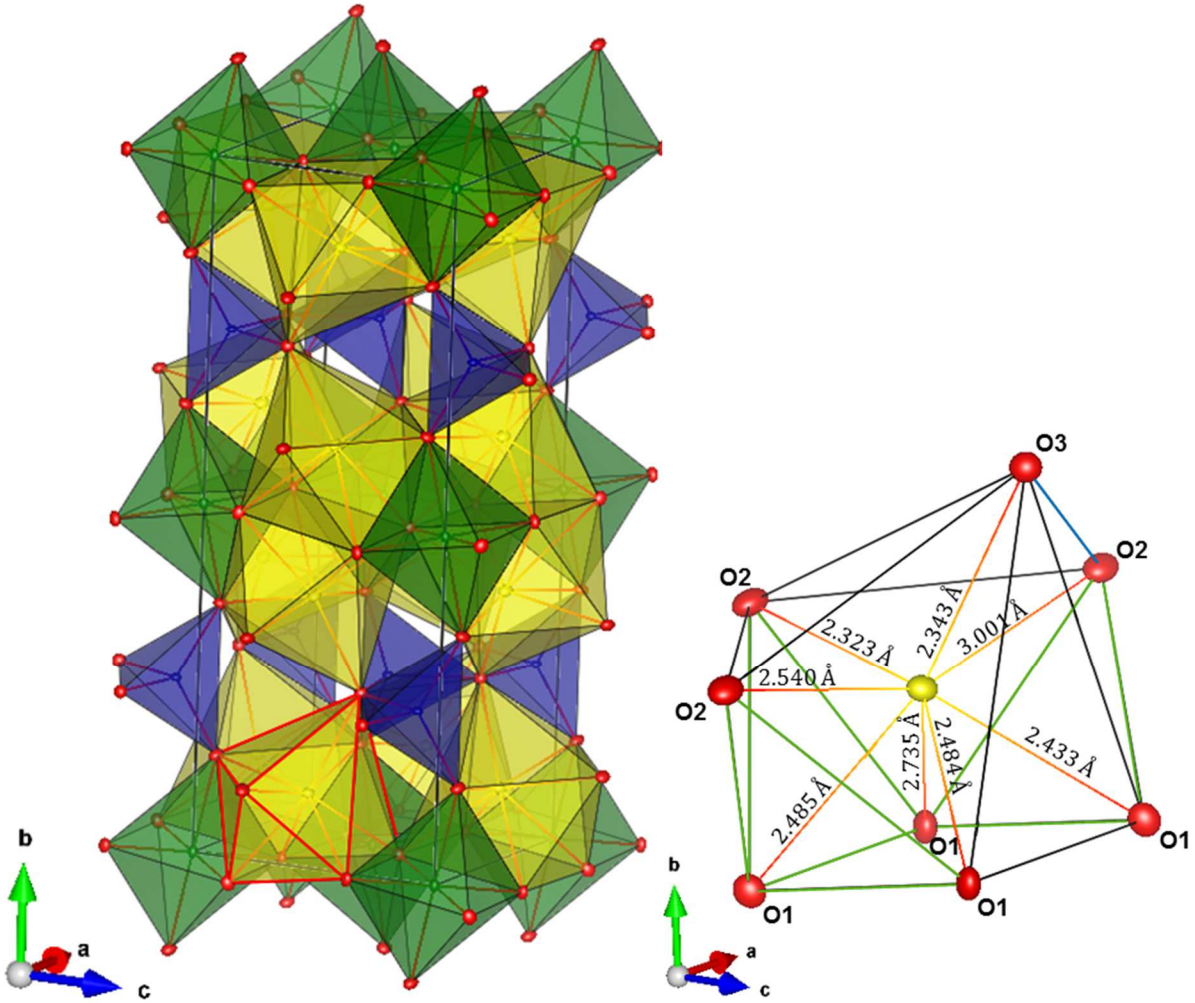


**Figure S16.** Polyhedral drawing of the Brownmillerite structure of pure $Ca_2Fe_2O_5$ in the *Pnma* phase, the coordination polyhedron about the $Ca^{2+}$ ion is red boarded (left side). On the right-handed side, an illustration of the distorted bicapped trigonal prism, with the Ca-O bond lengths is depicted

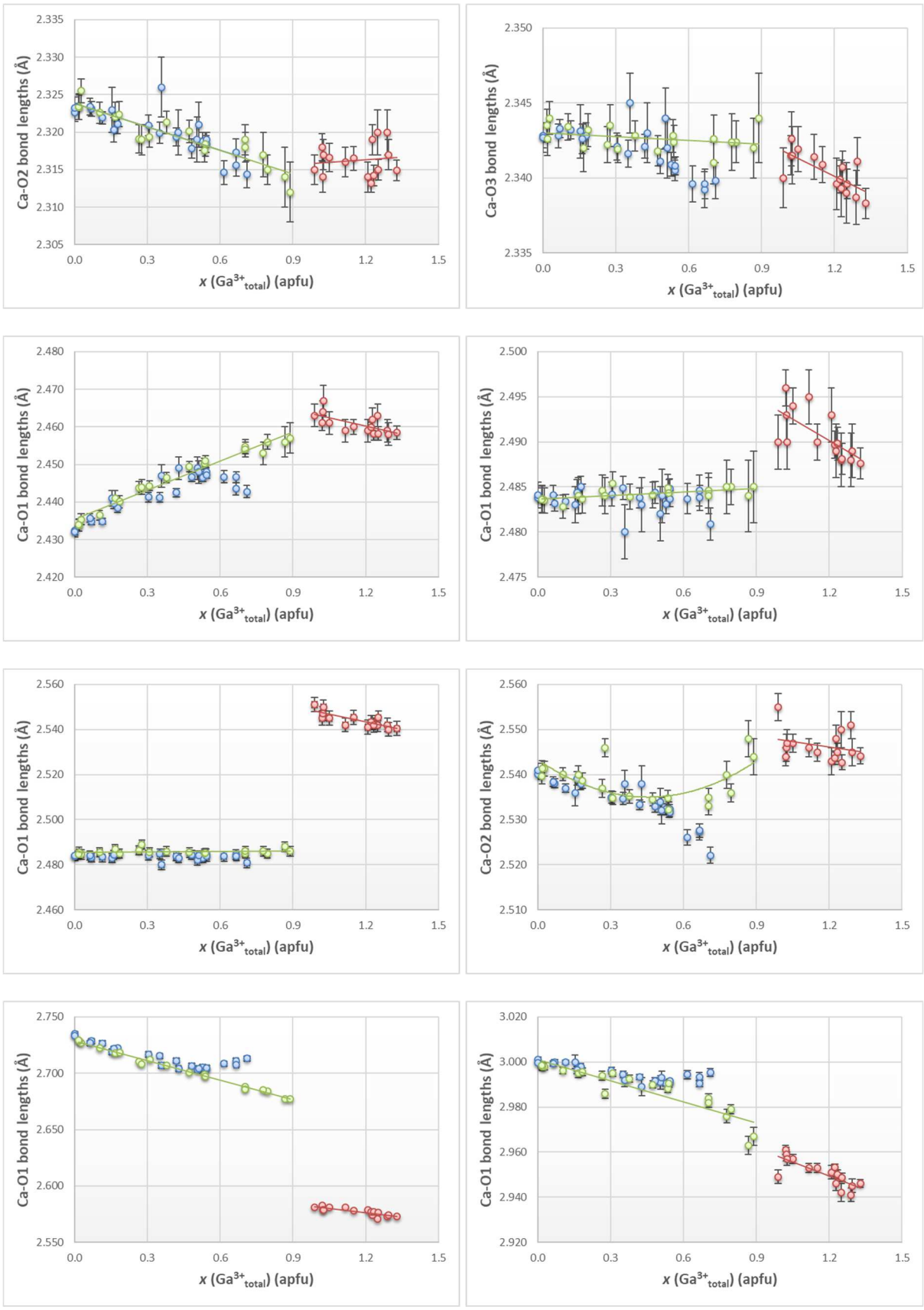


**Figure S17.** Individual Ca-O bond lengths (A-H) of the $Ca_2Fe_{2-x}Ga_xO_5$ solid solution series at 25 °C, symbols as in S9.

# 4 Definition of distortion parameters

The degree of polyhedral distortion can be characterized with distortion parameters defined by (Renner & Lehmann, 1986). One distortion parameter is the bond length distortion (BLD) and is based on the difference of the specific bond lengths and the average bond length and give converging results:

$$\mathrm{BLD} = \frac{100}{\mathrm{n}} \sum_{\mathrm{i}=1}^{\mathrm{n}} \frac{|(\mathrm{X}-\mathrm{O})_{\mathrm{i}} - \langle \mathrm{X}-\mathrm{O} \rangle|}{\langle \mathrm{X}-\mathrm{O} \rangle} \%$$

, where n is the number of bonds, $(X\text{-}O)_i$ is the individual and <X-O> the average X-O bond length.

In addition to the bond length distortion, (Renner & Lehmann, 1986) introduced the edge length distortion (ELD):

$$\mathrm{ELD} = \frac{100}{\mathrm{n}} \sum_{\mathrm{i}=1}^{\mathrm{n}} \frac{|(\mathrm{O}-\mathrm{O})_{\mathrm{i}} - \langle \mathrm{O}-\mathrm{O} \rangle|}{\langle \mathrm{O}-\mathrm{O} \rangle} \%$$

, where n is the number of bonds.

The quadratic octahedral angle variance OAV, as defined by (Robinson *et al.*, 1971), cover all O-M-O bond angles and is zero for a regular octahedron:

$$\mathrm{OAV} = \sum_{\mathrm{i}=1}^{12} \frac{(\Theta_i - 90°)^2}{11}$$

Finally, the quadratic tetrahedral angle variance TAV as defined by (Robinson *et al.*, 1971), cover all O-T-O bond angles and is zero for a regular tetrahedron:

$$\mathrm{TAV} = \sum_{\mathrm{i}=1}^{6} \frac{(\Theta_i - 109.47°)^2}{5}$$

# 5 Mössbauer spectroscopy

**Table S1:** Data evaluation strategy used for analysis of magnetically split Mössbauer spectra of $CaFe_{2-x}Ga_xO_5$ solid solution series compounds.

| | Octahedral site | Tetrahedral site |
|---|---|---|
| $\Delta E_q$ | positive | negative |
| θ | ~ 90° | = 90° (fixed) |
| ϕ | ~ - 10° | ~ 0° |
| η | ~ 0.25 | ~ 0 |
| ε | negative | positive |
| $V_{zz}$ | ~ // b | = // b |

$\Delta E_q$ = quadrupole splitting given by$\Delta = \frac{e^2qQ}{2}\sqrt{1+\frac{1}{3}\eta^2}$, θ = polar angle between $V_{zz}$ and the direction of the internal magnetic field $H_f$, ϕ = azimuthal angle between the projection of $H_f$ onto the xy plane of the EFG and $V_{zz}$, η = asymmetry parameter of the EFG with $\eta = \frac{(|V_{xx}|-|V_{yy}|)}{|V_{zz}|}$, ε = the quadrupole shift given by $\varepsilon = \frac{e^2qQ}{8}\left[2-\left(3-\eta cos2\phi_{Hq}\right)sin^2\theta_{Hq}\right]$.

Table S2: $^{57}Fe$ hyperfine parameter for samples of the $CaFe_{2-x}Ga_xO_5$ solid solution series, evaluated with the approach of the hyperfine field distribution fitting of spectra, parameters are defined in Table S1, σ = width of the Gaussian distribution of the hyperfine field, estimated standard deviations are smaller than 0.005 mm/s for Γ/2, δ, and ε, smaller than 0.5 kOe for $H_f$ and σ, and smaller than 0.5 % for the relative area fraction.

.

| | | | | Octahedral site | | | | | | | | |
|---|---|---|---|---|---|---|---|---|---|---|---|---|
| Sample | X(Ga) initial | Intern ID | Γ/2 (mm/s) | δ (mm/s) | ε (mm/s) | $H_f-1$ (kOe) | σ $H_f-1$ (kOe) | $H_f-2$ (kOe) | σ $H_f-2$ (kOe) | $H_f-3$ (kOe) | σ $H_f-3$ (kOe) | Area (%) |
| BGa0.0 | 0 | 30058 | 0.138 | 0.368 | -0.264 | 507.54 | 2.56 | -- | -- | -- | -- | 49.51 |
| BGa0.0 | 0 | 40017 | 0.148 | 0.365 | -0.260 | 509.91 | 1.82 | -- | -- | -- | -- | 50.49 |
| BGa0.1 | 0.1 | 30245 | 0.151 | 0.366 | -0.271 | 499.64 | 3.51 | -- | -- | -- | -- | 51.71 |
| BGa0.1 | 0.1 | 30403 | 0.149 | 0.364 | -0.275 | 502.13 | 4.61 | -- | -- | -- | -- | 52.60 |
| BGa0.2 | 0.3 | 21833 | 0.156 | 0.367 | -0.272 | 487.40 | 8.36 | -- | -- | -- | -- | 58.22 |
| BGa0.2 | 0.3 | 30246 | 0.174 | 0.368 | -0.265 | 483.02 | 9.40 | -- | -- | -- | -- | 58.38 |
| BGa0.3 | 0.2 | 30247 | 0.167 | 0.369 | -0.271 | 494.49 | 5.00 | -- | -- | -- | -- | 54.11 |
| BGa0.3 | 0.2 | 30404 | 0.170 | 0.368 | -0.278 | 494.92 | 6.01 | -- | -- | -- | -- | 54.42 |
| BGa0.4 | 0.4 | 21839 | 0.158 | 0.367 | -0.278 | 482.87 | 10.11 | -- | -- | -- | -- | 61.51 |
| BGa0.4 | 0.4 | 30248 | 0.178 | 0.368 | -0.269 | 483.50 | 8.84 | -- | -- | -- | -- | 61.93 |
| BGa0.5 | 0.5 | 30405 | 0.183 | 0.365 | -0.293 | 466.10 | 12.13 | -- | -- | -- | -- | 63.86 |

| | | | | | | | | | | | | |
|---|---|---|---|---|---|---|---|---|---|---|---|---|
| BGa0.5 | 0.5 | 11274 | 0.187 | 0.361 | -0.288 | 463.18 | 16.41 | -- | -- | -- | -- | 64.98 |
| BGa0.6 | 0.6 | 21836 | 0.186 | 0.364 | -0.403 | 453.38 | 15.45 | -- | -- | -- | -- | 67.84 |
| BGa0.7 | 0.7 | 21838 | 0.189 | 0.363 | -0.424 | 438.12 | 13.96 | 402.67 | 27.88 | -- | -- | 71.93 |
| BGa0.7 | 0.7 | 11277 | 0.332 | 0.364 | -0.416 | 441.04 | 8.09 | 402.00 | 15.00 | -- | -- | 70.16 |
| BGa0.8 | 0.8 | 11275 | 0.227 | 0.362 | -0.405 | 421.91 | 19.73 | 344.12 | 51.79 | -- | -- | 72.77 |
| BGa0.8 | 0.8 | 21837 | 0.150 | 0.363 | -0.423 | 421.74 | 15.85 | 383.91 | 23.52 | -- | -- | 72.19 |
| BGa0.9 | 0.9 | 21474 | 0.150 | 0.363 | -0.423 | 390.72 | 22.08 | 335.31 | 58.88 | -- | -- | 73.69 |
| BGa0.9 | 0.9 | 21834 | 0.150 | 0.360 | -0.418 | 387.08 | 20.43 | 348.16 | 29.50 | 279.30 | 52.52 | 73.30 |

| | | | Tetrahedral site | | | | | | | | |
|---|---|---|---|---|---|---|---|---|---|---|---|
| Sample | X(Ga) initial | Intern ID | δ (mm/s) | ε (mm/s) | $H_f-1$ (kOe) | σ $H_f-1$ (kOe) | $H_f-2$ (kOe) | σ $H_f-2$ (kOe) | $H_f-3$ (kOe) | σ $H_f-3$ (kOe) | Area (%) |
| BGa0.0 | 0 | 30058 | 0.181 | 0.361 | 432.2 | 1.5 | -- | -- | -- | -- | 50.5 |
| BGa0.0 | 0 | 40017 | 0.189 | 0.359 | 432.7 | 2.3 | -- | -- | -- | -- | 49.5 |
| BGa0.1 | 0.1 | 30245 | 0.190 | 0.361 | 432.4 | 1.2 | 403.0 | 0.0 | -- | -- | 48.3 |
| BGa0.1 | 0.1 | 30403 | 0.191 | 0.366 | 432.9 | 2.4 | 403.1 | 4.1 | -- | -- | 47.4 |
| BGa0.2 | 0.3 | 21833 | 0.189 | 0.370 | 423.6 | 2.4 | 395.4 | 4.8 | 341.6 | 1.0 | 41.8 |
| BGa0.2 | 0.3 | 30246 | 0.180 | 0.360 | 422.1 | 3.3 | 395.4 | 3.8 | 340.3 | 1.1 | 41.6 |

| | | | | | | | | | | | |
|---|---|---|---|---|---|---|---|---|---|---|---|
| BGa0.3 | 0.2 | 30247 | 0.188 | 0.370 | 429.2 | 0.0 | 398.4 | 6.6 | -- | -- | 45.9 |
| BGa0.3 | 0.2 | 30404 | 0.182 | 0.371 | 429.1 | 2.2 | 400.5 | 6.1 | -- | -- | 45.6 |
| BGa0.4 | 0.4 | 21839 | 0.187 | 0.372 | 419.0 | 0.2 | 391.6 | 6.1 | 338.1 | 3.0 | 38.5 |
| BGa0.4 | 0.4 | 30248 | 0.189 | 0.369 | 420.0 | 0.0 | 392.1 | 7.5 | 340.6 | 3.0 | 38.1 |
| BGa0.5 | 0.5 | 30405 | 0.186 | 0.373 | 411.4 | 1.3 | 386.6 | 4.5 | 333.7 | 0.0 | 36.1 |
| BGa0.5 | 0.5 | 11274 | 0.183 | 0.370 | 410.0 | 0.2 | 385.6 | 8.8 | 332.6 | 8.9 | 35.0 |
| BGa0.6 | 0.6 | 21836 | 0.185 | 0.340 | 403.2 | 0.2 | 376.8 | 6.5 | 325.2 | 1.2 | 32.2 |
| BGa0.7 | 0.7 | 21838 | 0.187 | 0.322 | -- | -- | 368.7 | 5.0 | 315.0 | 4.0 | 28.1 |
| BGa0.7 | 0.7 | 11277 | 0.182 | 0.334 | -- | -- | 367.9 | 15.0 | 314.6 | 10.0 | 29.8 |
| BGa0.8 | 0.8 | 11275 | 0.190 | 0.350 | -- | -- | 355.7 | 15.0 | 298.6 | 15.0 | 27.2 |
| BGa0.8 | 0.8 | 21837 | 0.187 | 0.344 | -- | -- | 357.1 | 10.9 | 302.1 | 13.7 | 27.8 |
| BGa0.9 | 0.9 | 21474 | 0.190 | 0.360 | -- | -- | 319.1 | -- | -- | -- | 26.3 |
| BGa0.9 | 0.9 | 21834 | 0.190 | 0.369 | -- | -- | 283.6 | 30.0 | -- | -- | 26.7 |

# 6 References


Abakumov, A. M., Kalyuzhnaya, A. S., Rozova, M. G., Antipov, E. V., Hadermann, J. & Van Tendeloo, G. (2005). *Solid State Sciences* **7**, 801-811.

Bielecki, J., Parker, S. F., Ekanayake, D., Rahman, S. M. H., Borjesson, L. & Karlsson, M. (2014). *Journal of Materials Chemistry A* **2**, 16915-16924.

Grosvenor, A. P., Ramezanipour, F., Derakhshan, S., Maunders, C., Botton, G. A. & Greedan, J. E. (2009). *Journal of Materials Chemistry* **19**, 9213-9220.

Krueger, H. (2007). *Dissertation, Uni Innsbruck*, 112.

Okrusch, M. (2014). Private communication.

Piovano, A., Ceretti, M., Johnson, M. R., Agostini, G., Paulus, W. & Lamberti, C. (2015). *Journal of Physics-Condensed Matter* **27**.

Redhammer, G. J., Amthauer, G., Tippelt, G., Lottermoser, W. & Roth, G. (2005). *Industrial Applications of the Mossbauer Effect*, edited by M. Gracia, J. F. Marco & F. Plazaola, pp. 179-184.

Renner, B. & Lehmann, G. (1986). *Zeitschrift Fur Kristallographie* **175**, 43-59.

Robinson, K., Gibbs, G. V. & Ribbe, P. H. (1971). *Science* **172**, 567-&.

Stølen, S., Bakken, E. & Mohn, C. E. (2006). *Physical Chemistry Chemical Physics* **8**, 429-447.

Tilley, R. J. D. (2016). *Wiley*, 328.

Young, J. & Rondinelli, J. M. (2015). *Physical Review B* **92**.